On the importance of the choice of the parameters of the Johnson-Cook constitutive model and their influence on the results of a Ti6Al4V orthogonal cutting model

F. Ducobu*, E. Rivière-Lorphèvre, E. Filippi

University of Mons (UMONS), Faculty of Engineering (FPMs), Machine Design and Production Engineering Lab, 20 Place du Parc, B-7000 Mons, Belgium

ARTICLE INFO

ABSTRACT

A wide range of parameters is available in the literature for the Johnson-Cook constitutive model, the most used flow stress in metal cutting modelling. This strength of the Johnson-Cook model is also a weakness as it is therefore difficult to choose the set that will provide the most accurate results. Indeed, for a given material, several parameters are available due to different identification conditions (strain, strain rates and temperature range). This paper gathers the sets of Johnson-Cook parameters from the literature for Ti6Al4V before comparing them based on their stress-strain curves. The twenty identified sets are then introduced in a Coupled Eulerian-Lagrangian (CEL) finite element orthogonal cutting model and their results are compared at fixed cutting conditions. This comparison is then extended for the three most characteristic sets to two other uncut chip thicknesses. All the numerical results are compared to an experimental reference in the same cutting conditions. Links between the parameters of the Johnson-Cook flow stress and outputs of the model are then highlighted; they are still valid when the uncut chip value is modified. A set is finally recommended to obtain an accurate estimation of the cutting force and average feed force and chip thickness values.

1. Introduction

Machining by removal of chips with a cutting tool is a process involving large strains and strain rates, as well as high temperatures, in the machined material. The numerical modelling is widely adopted to help understanding the numerous phenomena it involves. This complex manufacturing process is up to now mostly studied in the simplified orthogonal cutting configuration. The finite element method is frequently used to model the process with Lagrangian, Eulerian and Arbitrary Lagrangian Eulerian formulations. The newly introduced Coupled Eulerian-Lagrangian (CEL) formulation overcome many of their limitations and constitutes a promising alternative [1].

An accurate material constitutive model is a key issue to develop a realistic finite element model of a machining operation. It is therefore primordial to use a flow stress model able to take into account the specifities of the process. In metal cutting, it should ideally depends on the strain, the strain rate, the temperature, the hardening, the viscosity and the loading history of the material. So far, there is no constitutive model taking all these phenomena into account and simplifying hypothesis are introduced. Jeunechamp [2] and Hor [3] present an overview of the most used constitutive models (beyond the modelling of

machining by removal of chips) taking into account the strain rate.

The dynamic range, when the material properties are studied, is defined for strain rates larger than 1 s^{-1} [2]. Typical strain rates in machining are usually from 10^4 s^{-1} to 10^7 s^{-1} according to [4]. This leads metal cutting to be the forming process for which the strain rates are the largest [5]. Typical values for strains are up to 6 [4]. These values are so high that, so far, no experimental mean of test has been developed to reach these extreme conditions of strains and strain rates, what is more at sufficiently high temperatures. Empirical constitutive models are widely adopted although they only represent accurately the material for lower strains, strain rates and temperatures than what is observed during machining. The values used during the computation of the model are therefore extrapolated ones.

2. The Johnson-Cook constitutive model and its parameters

The Johnson-Cook flow stress [6] is the most used one in the finite element modelling of metal cutting. This empirical model dissociates plastic, viscous and thermal aspects without taking the strain softening into account as proposed by more recent models [7]. This phenomenon is however only significant when segmented (or serrated, saw-toothed)

---

chips are formed. The Johnson-Cook model is therefore well suited for continuous chip modelling and remains often adopted in the current literature [1,8–10]. The Johnson-Cook flow stress is given by

$$\sigma = (A + B\,\varepsilon^n)\left(1 + C\,\ln\frac{\dot{\varepsilon}}{\dot{\varepsilon}_0}\right)\left(1 - \left[\frac{T - T_{room}}{T_{melt} - T_{room}}\right]^m\right) \tag{1}$$

It involves five materials constants: the yield strength, *A*, the hardening modulus, *B*, the strain-hardening exponent, *n*, the strain rate sensitivity, *C*, and the thermal sensitivity, *m*. Constants *B* and *n* describe the strain hardening. T_{melt} and T_{room} are respectively the melting temperature and the room temperature, while $\dot{\varepsilon}_0$ is the reference strain rate. The term depending on the temperature is 0 when $T = T_{melt}$, meaning that it makes no sense to use the Johnson-Cook constitutive model for temperatures above T_{melt}. The term related to the viscosity is equal to 1 when the strain rate $\dot{\varepsilon}$ is equal to the reference value $\dot{\varepsilon}_0$ and the flow stress is independent of the strain rate at that particular strain rate.

The parameters of the Johnson-Cook constitutive model are generally determined by Split Hopkinson Pressure Bar (SPHB) [11]. That experimental configuration allows to reach strains up to 0.5 and strain rates lower than $10^4\,\text{s}^{-1}$ [12]. These values are lower than what is observed during machining. The flow stress for higher values is then extrapolated, which can lead to questionable evolutions. In the range of experimental values, the Johnson-Cook flow does however accurately represent the material behaviour [12]. According to Sima and Özel [13], the Johnson-Cook constitutive model does not represent accurately the behaviour of the material at high strain and the effects of strain, strain rate and temperature should be taken into account. Calamaz et al. [12] consider that the Johnson-Cook flow stress should not be adopted for strains larger than 0.3 and strain rates larger than $1000\,\text{s}^{-1}$.

With the friction at the tool – chip interface, the material constitutive model are the two major factors that influence the modelling of machining [14,15]. Filice et al. [16] investigated the influence of the material flow stress and friction law. Four constitutive models were considered, one of them being Johnson-Cook's, and three friction models, one of them is Coulomb's. They concluded that significant differences are observed depending on the material constitutive model and that there is not a single model that predicts accurately all the studied values (for example, the cutting force can be correctly modelled but then the feed force will not, and vice versa).

Umbrello et al. [17] performed a sensitivity study of the influence of the value of the Johnson-Cook parameters on the chip morphology, the forces, the temperatures and the residual stresses for AISI 316 L steel that they obtained from the finite element model they developed. Five sets of parameters were considered. One of the set gave better results than the others. However, they concluded that the measured outputs, and particularly the residual stresses, are very dependent on the value of the Johnson-Cook parameters. According to Umbrello et al. [17,18], the Johnson-Cook flow stress is not suited for large strains due to its identification with SPHB that cannot reach strains as large as in machining.

The same kind of study was performed by Umbrello [18] but for Ti6Al4V in conventional and high speed machining. The comparison involved three sets of parameters and concerned the chip morphology and the cutting force. According to the author, the quality of the results is closely linked to the identification conditions of the Johnson-Cook parameters, which should be as close as possible to that of machining. The recommended procedure consists in an identification based on the results of machining experiments or the combination of machining and SHPB experiments. The machining experiments give cutting forces that are introduced in an analytical orthogonal cutting model to determine the parameters of the Johnson-Cook flow stress for the material in the primary shear zone [19]. Such a procedure avoids the extrapolations caused by the limitation in strains, strain rates and temperatures of SPHB, increasing the accuracy of the numerical results.

In addition to the wide implementation of the Johnson-Cook model in commercial and industry-oriented finite element softwares, a noticeable advantage of this constitutive model is the large availability of its parameters for many materials in the literature. This strength is a weakness as well. Indeed, several sets of parameters are found in the literature for the same material and they can be very different. This variability is mainly due to the different experimental conditions, the chemical composition of the material and the thermal treatments. Khan et al. [20] pointed out the importance of the identification method followed to determine the parameters. They highlighted differences as large as 600% for some values used in the identification process although the chemical composition of the materials was the same.

The literature review showed no comparison between the sets of Johnson-Cook parameters prior to the finite element modelling of orthogonal cutting. The influence of these parameters on the stress-strain evolution and the numerical results was not observed either, although it should take part in the choice of a set of parameters. In this context, this paper proposes to collect different sets of Johnson-Cook parameters for an alloy widely used in machining in many industrial sectors, Ti6Al4V. All these sets will then be compared, based on their stress-strain evolutions. They will then be introduced in a previously validated finite element CEL model of 2D orthogonal cutting. The results will be compared based on the cutting and feed forces and the chip morphology. The comparison will bring the numerical results amongst themselves and with an experimental reference obtained in strictly orthogonal cutting conditions. These results and comparisons will be linked to the sets of parameters of the Johnson-Cook constitutive model in order to highlight the importance of the choice of the set and recommend the most suited one to obtain accurate results. The study will then be extended to two other cutting conditions for a short selection of the most significant sets of parameters.

3. Johnson-Cook model parameters for Ti6Al4V modelling of machining

3.1. Presentation of the sets of parameters

Table 1 gathers the twenty sets of Johnson-Cook parameters that were found in the literature for Ti6Al4V. They are ordered in ascending order of *A* value. It is immediately noted that the value of some parameters varies of more than 100% depending on the source. The very large variation of parameter *A*, the yield strength at room temperature, is very surprising as this value was expected to be known and quite constant. This leads to assume that when *A* is significantly different of the Ti6Al4V yield strength, the identifications were performed without taking the physical meaning of the parameters into account. Due to the large number of parameters to identify and the missing constraints on them, this however does not mean that the flow stress will not accurately represent the behaviour of the material.

It is also important to emphasise the difficulty to obtain complete information on the conditions taking part in the identification of the parameters, whether it is experimental conditions (slightly more than half of them is given in Table 1) or the exact chemical composition of the alloy or its thermal treatments (hardly ever given as in [20], for example). It may besides be possible that all the sets do not strictly represent the same material. This is all more critical that the literature review highlighted their influence on the results. Moreover, many authors do not give the value of $\dot{\varepsilon}_0$. In the absence of information in the literature, it is fixed to $\dot{\varepsilon}_0 = 1\,\text{s}^{-1}$, its default value [2]. This hypothesis was followed to complete Table 1 when it was necessary.

3.2. Analysis of the sets of parameters

The evolutions of the stresses of the twenty stets are plotted in Fig. 1 at a temperature of 773 K and a strain rate of 10,000 s^{-1}, typical values in metal machining. Many information are shown on that figure and it

Table 1

Sets of parameters of the Johnson-Cook constitutive model for Ti6Al4V and experimental conditions used to determine them, by ascending order of A ($\stackrel{+}{\cdot}$: no value specified by the authors and assumed equal to 1 as suggested by Jeunechamp [2] among others).

Set	Parameters						Experimental conditions			
	A (MPa)	B (MPa)	C	n	m	$\dot{\varepsilon}_0$ (s^{-1})	ε_{max}	$\dot{\varepsilon}_{max}$ (s^{-1})	T_{max} (K)	Comments
1 [21]	418.4	394.4	0.035	0.47	1	1$\stackrel{+}{\cdot}$	–	–	–	–
2 [22]	724.7	683.1	0.035	0.47	1	10^{-5}	0.35	3000	1373	SHPB
3 [23]	782.7	498.4	0.028	0.28	1	10^{-5}	0.3	2000	1373	SHPB
4 [24]	804	545	0.05	0.362	1.04	1$\stackrel{+}{\cdot}$	–	–	–	Numerical method
5 [25]	859	640	0.000022	0.22	1.1	1$\stackrel{+}{\cdot}$	–	–	–	–
6 [26]	862.5	331.2	0.012	0.34	0.8	1	0.57	2150	T_{room}	SPHB
7 [27]	870	990	0.008	1.01	1.4	1	–	–	–	Analytical model
8 [12]	870	990	0.011	0.25	1	1$\stackrel{+}{\cdot}$	–	–	–	–
9 [28]	881	468	0.039	0.122	0.7	1$\stackrel{+}{\cdot}$	–	–	–	–
10 [24]	884	599	0.034	0.362	1.04	1$\stackrel{+}{\cdot}$	–	–	–	Numerical method
11 [29]	896	656	0.0128	0.5	0.8	1	0.57	2150	T_{room}	SHPB
12 [30]	968	380	0.0197	0.421	0.577	0.1	–	1000	873	SHPB
13 [31]	983	348	0.024	0.32	0.69	0.1	–	10,000	1273	Inverse method
14 [32]	984	520.3	0.015	0.5102	0.8242	1$\stackrel{+}{\cdot}$	0.12	577.4	293	SHPB
15 [24]	988	762	0.015	0.414	1.51	1$\stackrel{+}{\cdot}$	–	–	–	Numerical method
16 [33]	997.9	653.1	0.0198	0.45	0.7	1	0.25	1400	1273	SPHB
17 [20]	1080	1007	0.01304	0.5975	0.7701	1	0.25	1700	755	SHPB
18 [34]	1098	1092	0.014	0.93	1.1	1	0.6	10,000	T_{room}	SHPB
19 [20]	1104	1036	0.0139	0.6349	0.7794	1	0.25	1700	755	SHPB
20 [35]	1119	838.6	0.01921	0.4734	0.6437	1$\stackrel{+}{\cdot}$	0.6	7000	1000	SHPB

Fig. 1. Stress-strain curves of the twenty sets at T=773 K and $\dot{\varepsilon}_0 = 10,000$ s^{-1}.

Fig. 2. Stress-strain curves of sets 2, 7, 15, 17, 18 and 19 at T=773 K and $\dot{\varepsilon}_0 = 10,000$ s^{-1}.
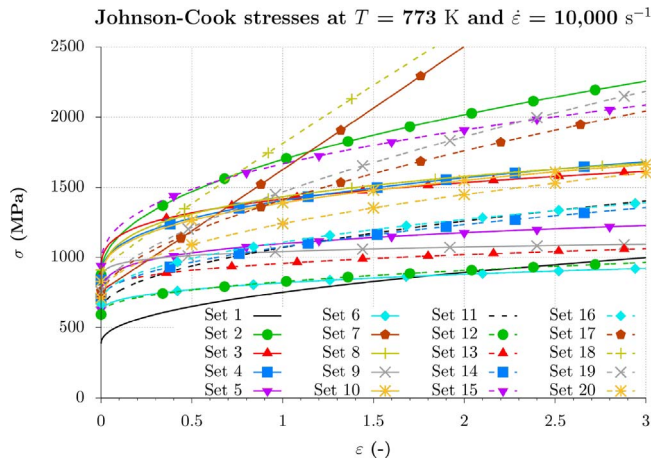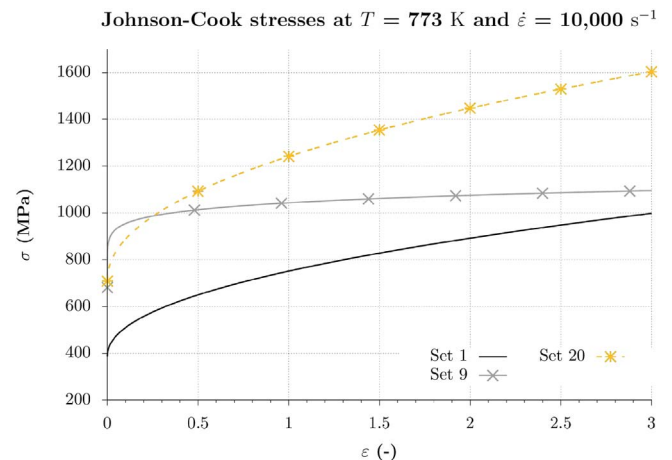

Fig. 3. Stress-strain curves of sets 1, 9 and 20 at T=773 K and $\dot{\varepsilon}_0 = 10,000$ s^{-1}.

is not easy to clearly identify each curve. The objective of this figure is to present a global view of the twenty sets. As for the parameters, significant differences are noted although the material is the same. When looking at the envelope of the curves, differences of a factor around 5 are observed between the stresses from the lower boundary and the stresses from the upper boundary. This upper boundary is defined by 2 particular sets for strains larger than 0.75. Their evolution differs from the others that are globally similar with a shape looking like a kind of logarithm (the exponent n inferior to 1 gives this shape). The lower boundary has as well a distinct evolution but with a logarithm-like shape. Some of the sets lead to evolutions and stresses that are nearly the same. A more detailed analysis is therefore required.

When looking closer to the stresses evolutions, smaller groups of sets can be identified. Sets 7 and 18 (Fig. 2) lead to high stresses with a nearly linear evolution. They are almost parallel and set 18 gives higher stresses mostly because of its higher A value. These very high stresses are due to B close to 1 GPa combined to a large n value. A n nearly equal to 1 leads to their nearly linear stresses evolutions. These n values are the highest of Table 1. The level of the stresses of sets 2 and 15 (Fig. 2) is the largest one when the evolution looks like a logarithm. Both are rather close at low strains and set 2 gives higher stresses at large strains mainly because of larger n and C values. Sets 17 and 19 (Fig. 2) also
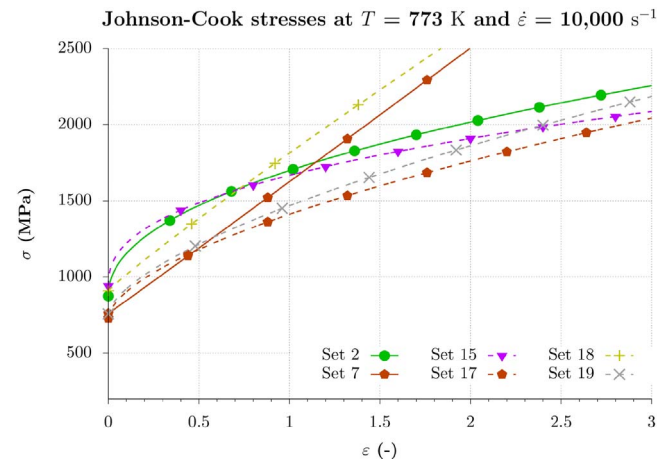
lead to high stresses. Their increase with strain is larger than the two previous ones, which is explained by their high n values. Set 19 increases more than set 17 because of its larger n value.
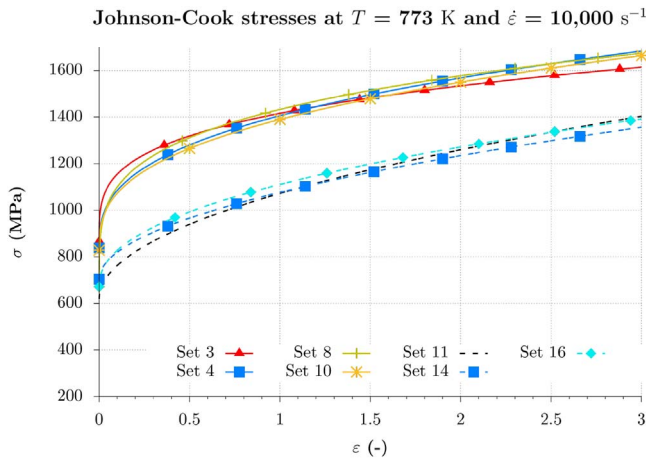
Fig. 4. Stress-strain curves of sets 3, 4, 8, 10, 11, 14 and 16 at $T=773$ K and $\dot{\varepsilon}_0 = 10,000$ s^{-1}.

Fig. 6. Stress-strain curves of sets 3, 4, 8, 10, 11, 14 and 16 at $T=673$ K and $\dot{\varepsilon}_0 = 10,000$ s^{-1}.

Fig. 7. Stress-strain curves of sets 3, 4, 8, 10, 11, 14 and 16 at $T=873$ K and $\dot{\varepsilon}_0 = 10,000$ s^{-1}.

At the opposite (Fig. 3), set 1 gives the lowest stresses at low strains due to small A and B values, coupled to a n value significantly lower than 1. The flow stress produced by set 9 (Fig. 3) has a shape that stands out the others. Indeed, after an initial increase, the stresses are nearly independent of strain. This is linked to the very low n value, the lowest of Table 1.

In Fig. 4, sets 3, 4, 8 and 10 exhibit very similar evolutions and stresses levels, as well as sets 11, 14 and 16 but at a lower level of stresses. The flow stresses of sets 11, 14 and 16 are lower than that of sets 3, 4, 8 and 10. When looking at both small groups, it is evident that B and n are such that their lower B value balances their higher n value, and vice versa.

Flow stresses curves of sets 6 and 12 are very close (Fig. 5). The lower n value of set 6 ends in a lower stress value at high strains. Evolutions of sets 5, 12 and 13 are nearly parallel. Set 5 is higher like its B value. When comparing set 12 and set 13, lower m and C values for set 12 give lower stresses.

The flow stresses evolutions and levels are now observed at different temperatures and strain rates. When temperature increases from 673 K to 773 K and 873 K (Figs. 6 and 7 and Figs. 8 and 9), the level of stresses decreases as expected from Eq. (1), highlighting the thermal softening. It is interesting to point out that the evolutions dot not change much and that the small groups formed at 773 K are not affected by the temperatures variations.

The stresses increase when strain rate goes from 1000 s^{-1} to 10,000 s^{-1} and 100,000 s^{-1} and the strain rate hardening is highlighted (Figs. 10 and 11 and Figs. 12 and 13). In Figs. 10 and 11, small
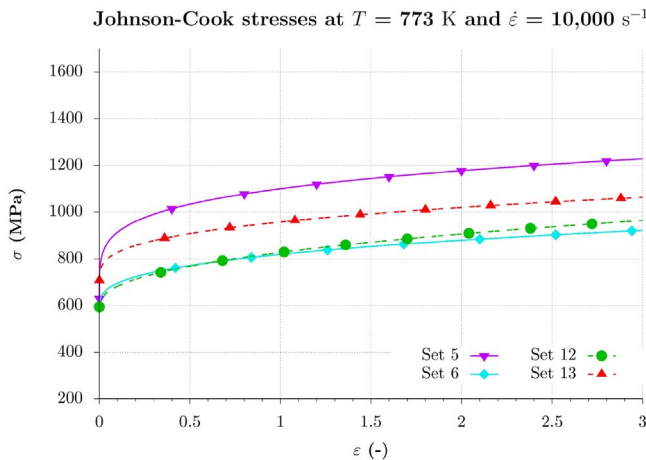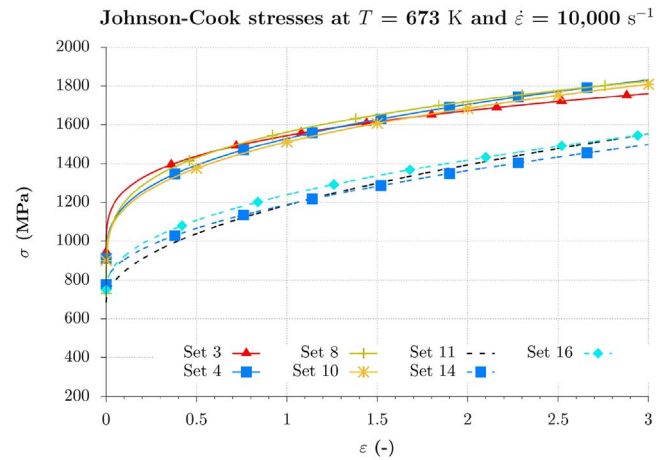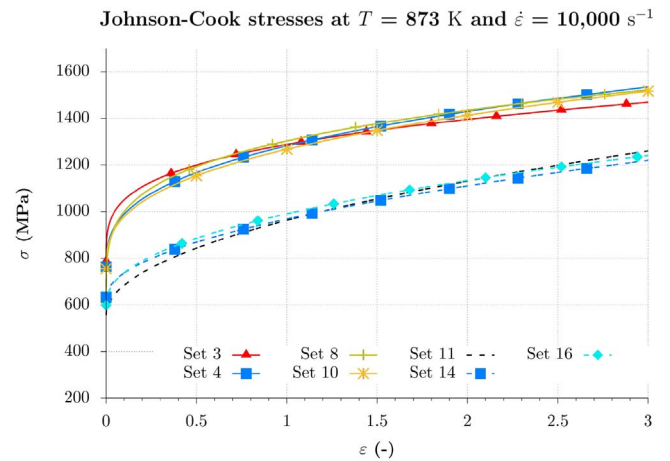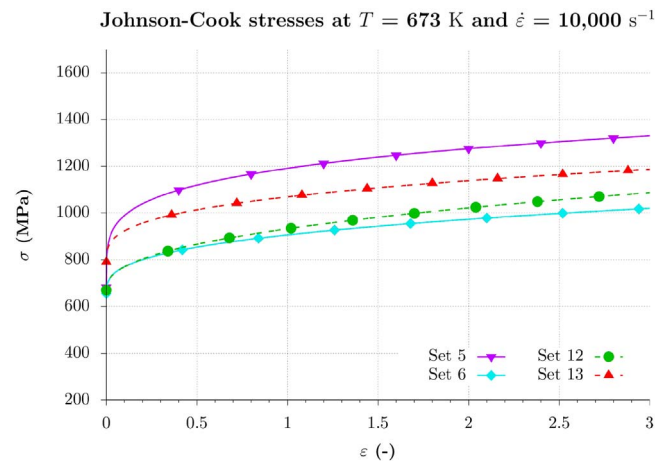

Fig. 8. Stress-strain curves of sets 5, 6, 12 and 13 at $T=673$ K and $\dot{\varepsilon}_0 = 10,000$ s^{-1}.

changes are noticed for sets 4 and 8 for example. At 1000 s^{-1}, stresses of set 8 are larger than that of set 4, while it is the contrary at 100,000 s^{-1}. This is due to the value of C larger for set 4 than for set 8. Stresses of set 5 in Figs. 12 and 13 are nearly insensitive to the level of strain rate, which is explained by the value of C nearly equal to 0 (it is 3 orders of magnitude lower than for all the other sets).
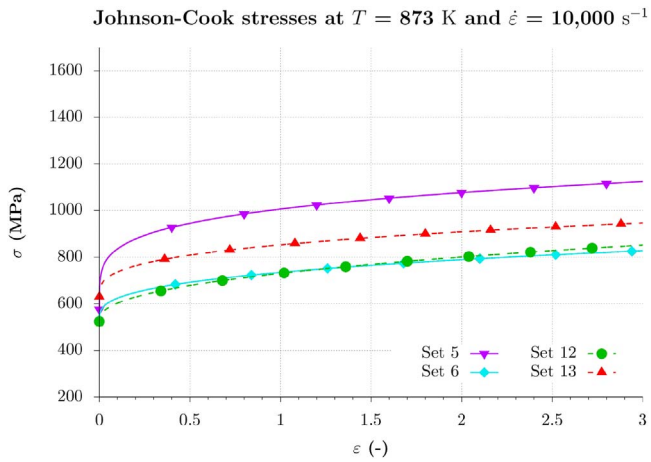

Fig. 5. Stress-strain curves of sets 5, 6, 12 and 13 at $T=773$ K and $\dot{\varepsilon}_0 = 10,000$ s^{-1}.
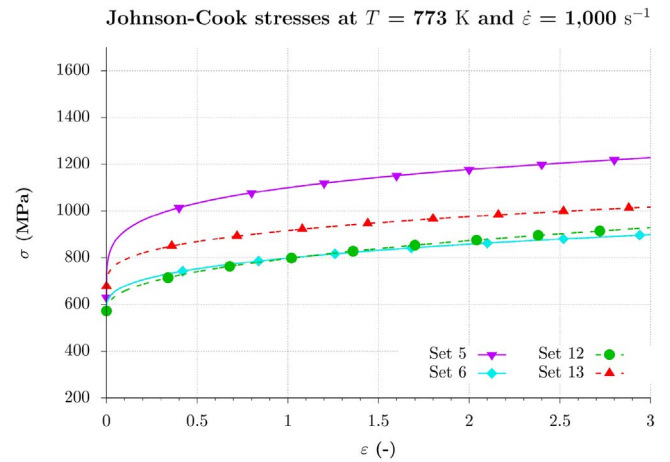
Fig. 9. Stress-strain curves of sets 5, 6, 12 and 13 at $T=873$ K and $\dot{\varepsilon}_0 = 10,000$ s^{-1}.

Fig. 12. Stress-strain curves of sets 5, 6, 12 and 13 at $T=773$ K and $\dot{\varepsilon}_0 = 1,000$ s^{-1}.
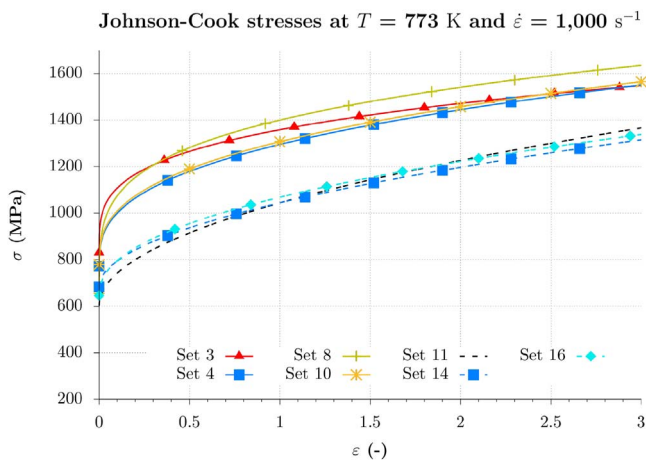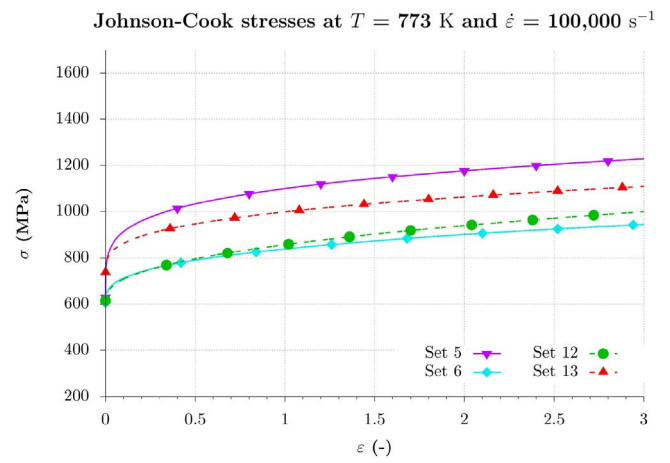

Fig. 10. Stress-strain curves of sets 3, 4, 8, 10, 11, 14 and 16 at $T=773$ K and $\dot{\varepsilon}_0 = 1,000$ s^{-1}.

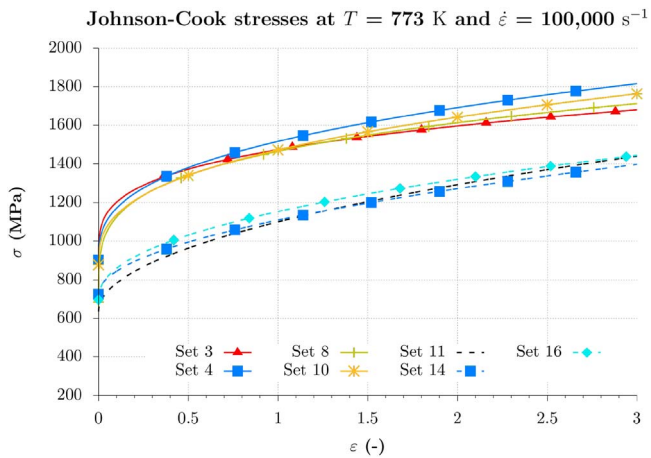**Fig. 13.** Stress-strain curves of sets 5, 6, 12 and 13 at $T=773$ K and $\dot{\varepsilon}_0 = 100,000$ s^{-1}.

Table 2
Cutting conditions and tool geometry [36].

Cutting speed, V_c (m/min)	30
Uncut chip thickness, h (μm)	40, 60, 100
Rake angle, γ (°)	15
Clearance angle, α (°)	2
Cutting edge radius, r (μm)	20

Fig. 11. Stress-strain curves of sets 3, 4, 8, 10, 11, 14 and 16 at $T=773$ K and $\dot{\varepsilon}_0 = 100,000$ s^{-1}.

Table 3
Experimental cutting (CF) and feed (FF) forces average RMS values, chip thickness (h') average values [36].

h (μm)	RMS CF (N/mm)	RMS FF (N/mm)	h' (μm)
40	86 ± 2	40 ± 1	59 ± 5
60	113 ± 2	44 ± 1	80 ± 4
100	174 ± 2	50 ± 1	135 ± 6

4. Experimental reference

Experimental tests were carried out to provide a reference for the numerical modelling. The setup, introduced in [36], allows to achieve plane strain 2D orthogonal cutting conditions on a common milling machine. Several cutting conditions were considered. The cutting speed was fixed to the maximal feed rate of the machine: 30 m/min and three uncut chip thicknesses were selected: 40 μm, 60 μm and 100 μm. At least three repetitions were performed. The cutting conditions of the experiments are summarized in Table 2.

The average of the root mean square (RMS) values of the cutting forces, measured with a Kistler dynamometer 9257B, are provided in Table 3. The chips were continuous for all the cutting conditions. Their thickness was measured on 25 points distributed along their length. The average values are summarized in Table 3. Standard deviations of both the forces and the chip thickness are low; they stay under 10% of the average value.
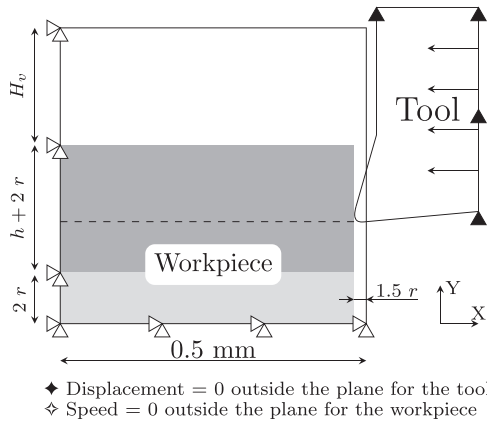
Fig. 14. Schematic initial geometry and boundary conditions of the model (*r*: cutting edge radius, *h*: uncut chip thickness, H_v: height of the area initially filled with void).
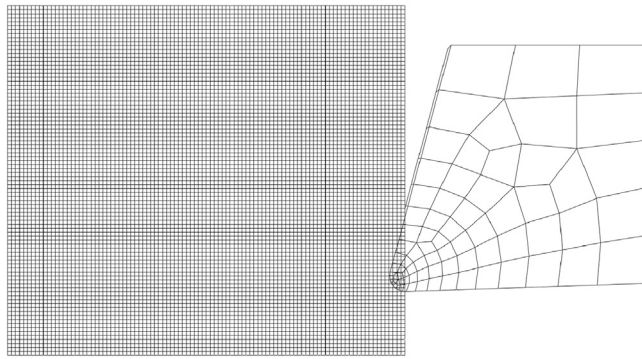

Fig. 15. Initial mesh of the model when $h = 60$ μm.

Table 4
Materials properties of the numerical models [29,38–42].

Young's modulus, E (GPa)	Ti6Al4V	113.8
	Carbide	800
Density, ρ (kg/m^3)	Ti6Al4V	4,430
	Carbide	15,000
Conductivity, k (W/mK)	Ti6Al4V	7.3
	Carbide	46
Expansion, α (K^{-1})	Ti6Al4V	8.6 e^{-6}
	Carbide	4.7 e^{-6}
Specific heat, c_P (J/KgK)	Ti6Al4V	580
	Carbide	203
Friction coefficient		0.2
Friction energy to heat (%)		100
Inelastic heat fraction		0.9
Heat partition to part (%)		50

5. CEL finite element model

The formulation adopted is the CEL. The Ti6Al4V orthogonal cutting model has been introduced and experimentally validated in [1]. As suggested by its name, the Lagrangian (for the tool) and Eulerian (for the workpiece) formulations are both employed, which allows to avoid severe mesh distortion in the workpiece due to the large strains. Its main drawback is the need for a larger number of elements in the mesh of the workpiece as it includes the area where the chip will form (the space initially filled with void above the workpiece).

Due to the restriction concerning the availability of element types in Abaqus/Explicit v6.14–2 [37] for the CEL formalism, 3D elements compose the model, with only one element in the direction perpendicular to the cutting plane in order to limit the number of degrees of freedom. The length of the workpiece, 0.5 mm, has been chosen to reach the steady-state of the cutting forces and a chip sufficiently long
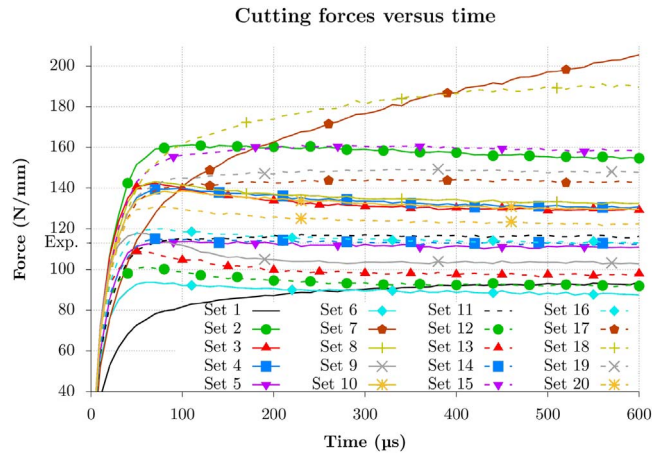

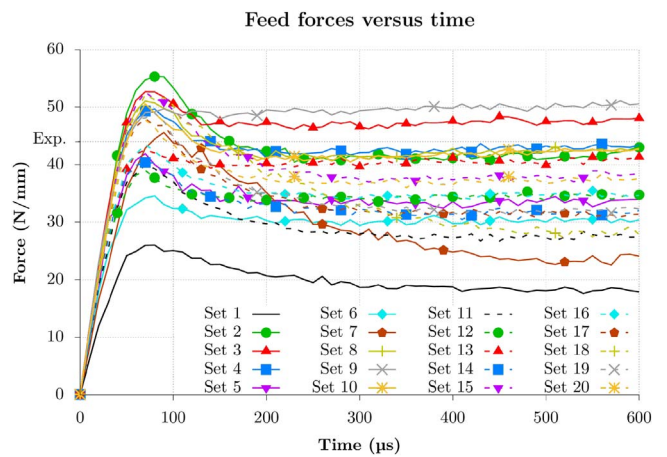**Fig. 16.** Cutting forces of the twenty sets for $h = 60$ μm after 600 μs of cutting.

Fig. 17. Feed forces of the twenty sets for $h = 60$ μm after 600 μs of cutting.

Table 5
RMS cutting forces and chip thickness summary for $h = 60$ μm, Δ_x: difference with the experimental values.

Case	CF (N/mm)	Δ_{CF} (%)	FF (N/mm)	Δ_{FF} (%)	h' (μm)	$\Delta_{h'}$ (%)
Exp.	113 ± 2	–	44 ± 1	–	80 ± 4	–
Set 1	92	18	18	60	114 ± 1	−43
Set 2	156	−47	42	14	105 ± 1	−31
Set 3	130	−11	48	−9	92 ± 1	−15
Set 4	131	−14	**43**	**3**	95 ± 1	−19
Set 5	111	1	33	25	104 ± 1	−30
Set 6	89	22	30	42	97 ± 0	−21
Set 7	192	−89	24	67	>115	>44
Set 8	133	−11	42	8	99 ± 0	−24
Set 9	103	7	50	−14	**76 ± 1**	**5**
Set 10	130	−17	42	4	97 ± 1	−21
Set 11	116	−2	27	40	109 ± 2	−36
Set 12	92	18	34	36	92 ± 0	−15
Set 13	98	17	40	10	**85 ± 1**	**−6**
Set 14	**113**	**0**	31	32	104 ± 1	−30
Set 15	159	−41	38	20	111 ± 2	−39
Set 16	**114**	**0**	34	26	99 ± 0	−24
Set 17	144	−27	31	38	112 ± 3	−40
Set 18	188	−52	29	48	115 ± 6	−44
Set 19	148	−19	32	43	112 ± 3	−40
Set 20	123	−7	37	23	100 ± 0	−25

to be measured, while keeping the number of nodes as low as possible. The dimensions of the workpiece and the boundary conditions of the model are schematically presented on Fig. 14.
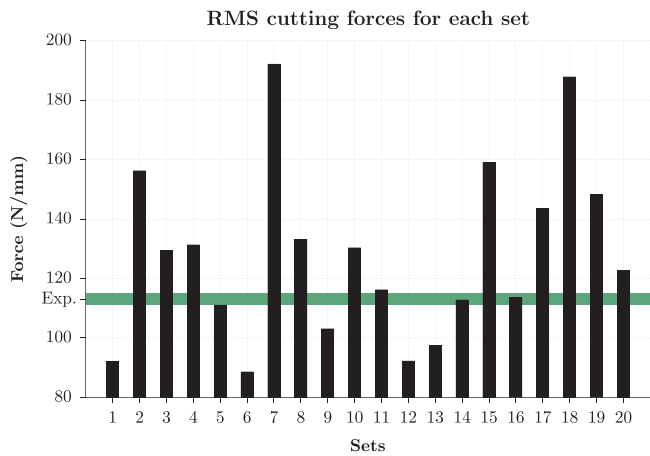
Fig. 18. Numerical and experimental RMS cutting forces for $h = 60\,\mu m$ after 600 μs of cutting (the experimental reference is shown with its standard deviation interval).
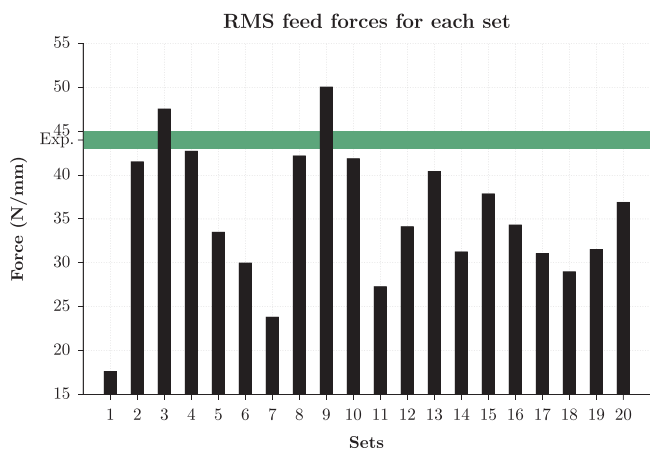

Fig. 19. Numerical and experimental RMS feed forces for $h = 60\,\mu m$ after 600 μs of cutting (the experimental reference is shown with its standard deviation interval).

The workpiece is meshed with 5 μm × 5 μm square (in the cutting plane) 8-node brick elements leading to a model of 8,800 elements and 17,978 nodes for the uncut chip thickness of 60 μm (H_v, the height of the area initially filled with void is 300 μm). The elements of the tool do not have a square shape in the cutting plane. Their length is 5 μm for the elements composing the edge radius and it increases with the distance to the radius. The mesh of the tool has 188 nodes and 75 elements. The initial mesh of the model when $h = 60$ μm is provided in Fig. 15.

The machined material, Ti6Al4V, is described by the Johnson-Cook constitutive model and the tool material, tungsten carbide, by a linear elastic model. 90% of the deformation energy is converted into heat.

Rech et al. [38] experimentally determined the value of the Coulomb coefficient at the tool – chip interface as 0.2. All of the friction energy is converted into heat and is equally allocated to the workpiece and the tool. Their faces are all adiabatic. The model characteristics are provided in Table 2 and the materials properties in Table 4.

6. Results

6.1. Forces

The cutting forces evolutions are plotted in Fig. 16. Similarly to the global view of the flow stresses, only 3 curves have a distinct evolution: the upper and lower boundaries of the envelope. Both are the same sets as for the stresses plot (Fig. 1). After an initial increase, whose shape can slightly vary depending on the small group of sets, the cutting forces are close to a constant (only the cutting force of set 7 is not constant). This confirms that the 600 μs modelled are sufficient to reach the steady-state of the forces. This cutting force evolution is linked to the type of chip produced: a continuous one. The comparison with the RMS experimental value shows that it is roughly in the middle of the range Fig. 17.

Concerning the feed force, all the sets give again similar evolutions. This time, the lower boundary of the envelope is clearly seen; it is the same set as for the cutting force and the flow stress plot. The upper boundary, although easily identified, is not constituted of the same sets as previously. After an initial increase followed by a decrease of variable magnitude depending on the set considered, the force is nearly constant. The RMS experimental value is close to the upper boundary. Nearly all the sets lead to a feed force lower than the experiments.

The RMS values of the forces are given in Table 5 with the experimental reference.

Figs. 18 and 19 are introduced to help the analysis with the experimental reference. For the cutting force, the numerical values are rather well distributed around the experimental reference. Two sets give values lying in the mean experimental value ± standard deviation interval: sets 14 and 16; bot are equal to the mean experimental value. Set 11 is just above, while set 5 is just below. Sets 6 and 1 lead to the smaller RMS cutting forces and sets 7 and 18 to the larger ones. A link can therefore clearly be made between the level of the stresses and the cutting forces RMS values. The two sets with the lower stresses produce the lower cutting forces values and the two higher RMS values are given by the two sets with the higher stresses. Stresses of sets 14 and 16 were in the middle of the range.

Concerning the feed forces, as expected from Fig. 19, the numerical values are globally much less accurately evaluated, which is common when modelling the cutting process. The two sets closer to the experiments are set 4 and set 8; not the same sets as for the cutting forces. The lowest value is provided by set 1 which already gave a low cutting force value. Surprisingly, the feed forces for sets 7 and 18 are rather low (their cutting forces values were the highest). It is conse-
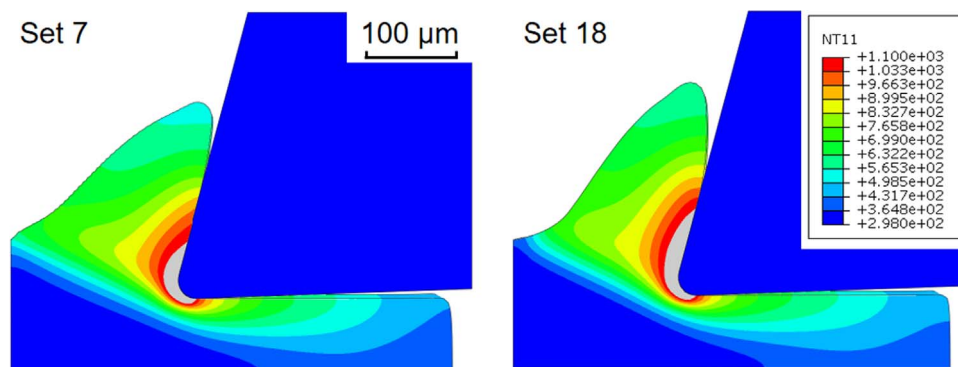

Fig. 20. Temperature contours (in K) of the numerical chips of sets 7 and 18 for $h = 60$ μm after 600 μs of cutting.

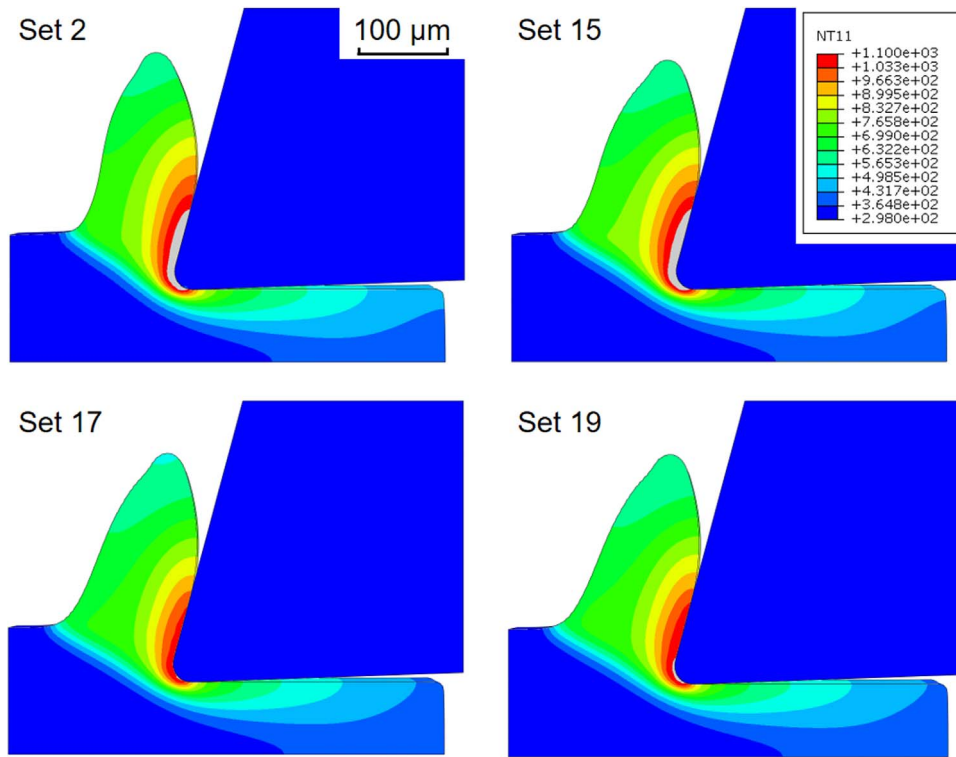**Fig. 21.** Temperature contours (in K) of the numerical chips of sets 2, 15, 17 and 19 for $h = 60$ µm after 600 µs of cutting.

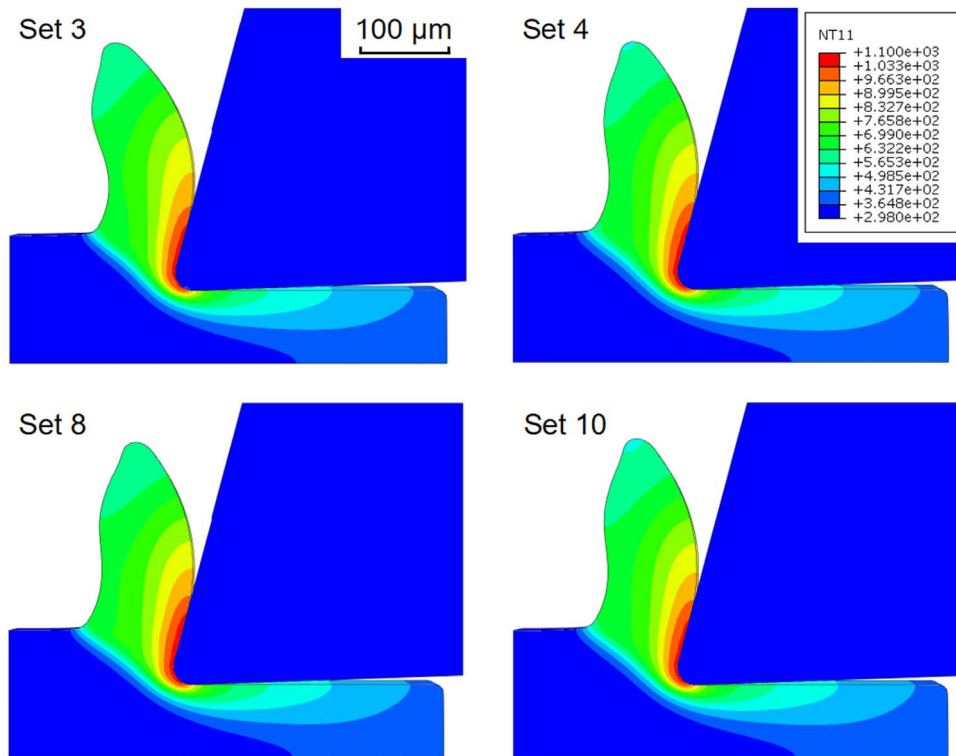**Fig. 22.** Temperature contours (in K) of the numerical chips of sets 3, 4, 8 and 10 for $h = 60$ µm after 600 µs of cutting.

quently rather hard to make a link between the flow stress and the RMS value of the feed force.

6.2. Chip morphology

Similarly to the analysis of the stress-strain evolutions, the chips morphologies are analysed in small groups (which are the same as

previously). All the numerical chips are continuous, as the experimental reference and expected from the previous evolutions. Differences are however noted. The chip thickness values of the twenty models are summarized in Table 5. Chips of sets 7 and 18 (Fig. 20) are the thickest ones. The thickness of chip 7 could not be measured because it has not reached its steady-state yet (this had already been noted in Fig. 16), highlighting that it would be thicker than chip 18. When looking at the
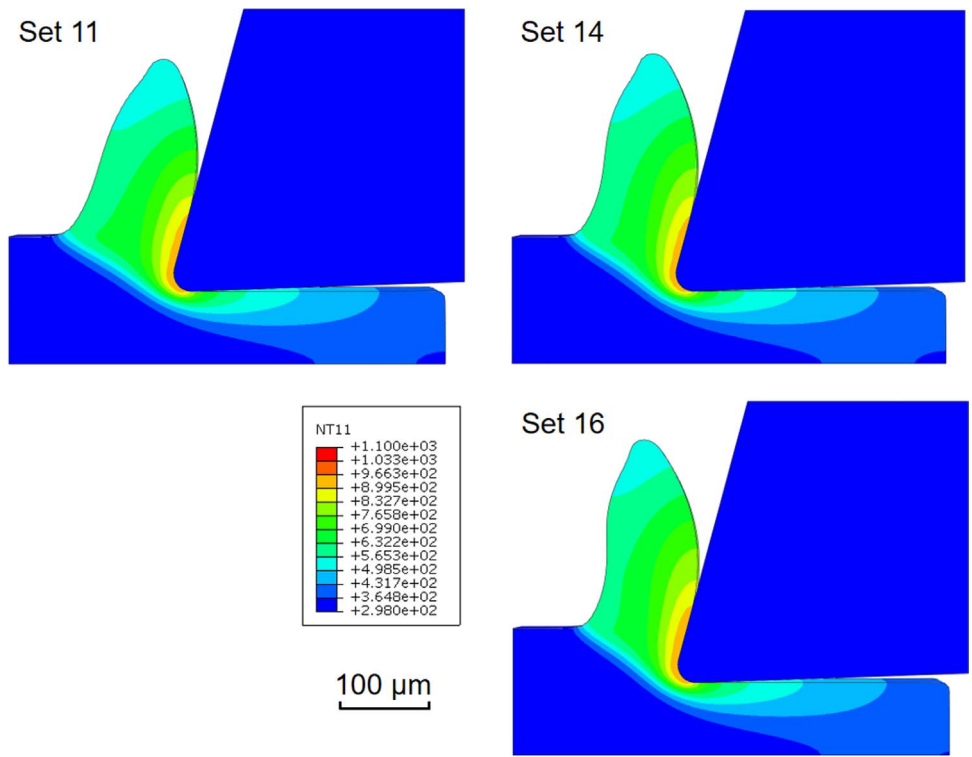
Fig. 23. Temperature contours (in K) of the numerical chips of sets 11, 14, 16 for $h = 60$ μm after 600 μs of cutting.
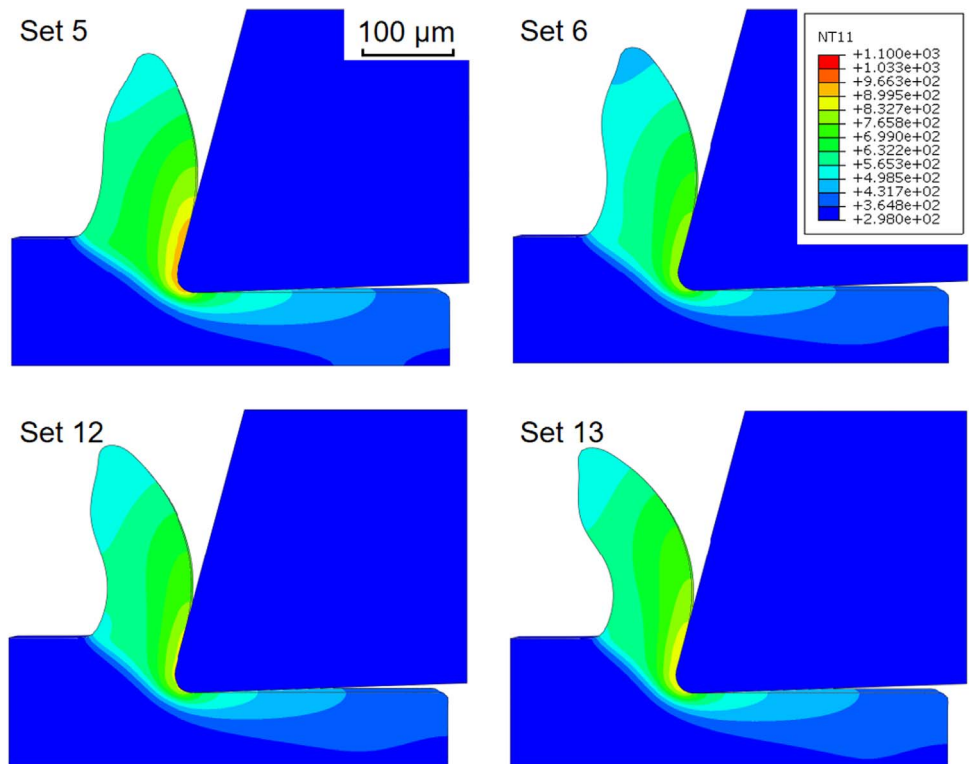

Fig. 24. Temperature contours (in K) of the numerical chips of sets 5, 6, 12 and 13 for $h = 60$ μm after 600 μs of cutting.

RMS forces values, they were the largest for the cutting forces and in the lower range for the feed forces. As expected, the secondary shear zone is the area where the temperature is maximal. The temperatures for these two sets are the highest which is explained by the higher level of stresses (and of cutting forces) their parameters lead to.

The temperature level of sets 2, 15, 17 and 19 (Fig. 21) is directly

linked to the level of the RMS cutting forces. The thicknesses of these four chips are just below the maximal value. Chip 2 is slightly thinner and its RMS feed force value is higher.

Chips 3, 4, 8 and 10 (Fig. 22) are in the lower range of thicknesses but their feed forces are nearly the largest. The chip thickness seems therefore inversely linked to the RMS feed force. The temperatures in
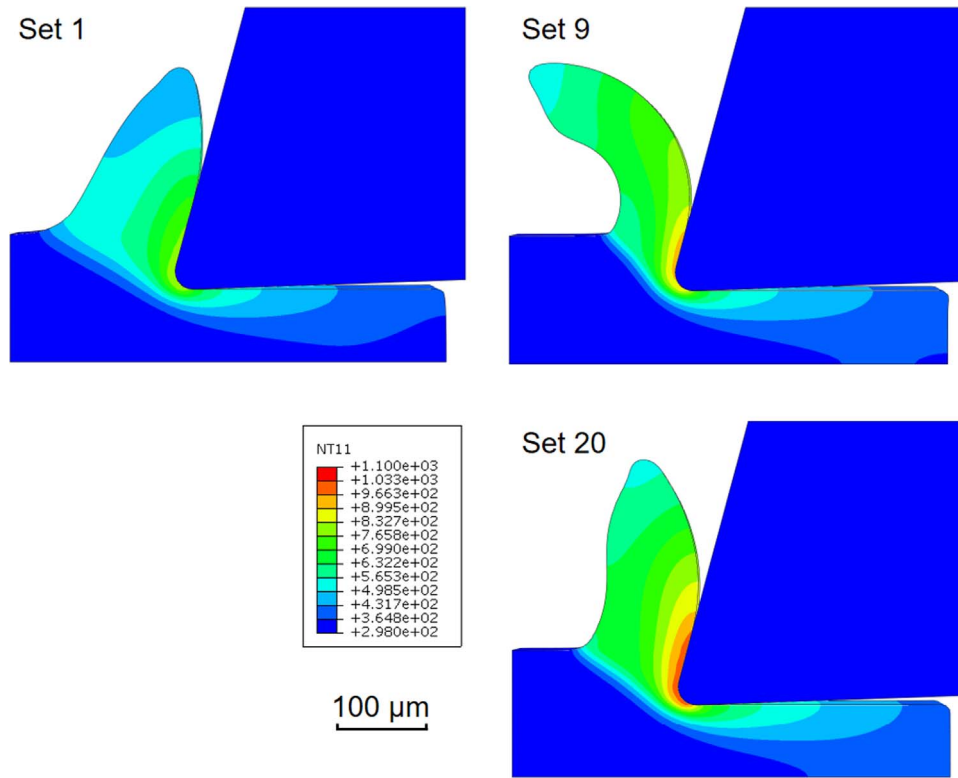
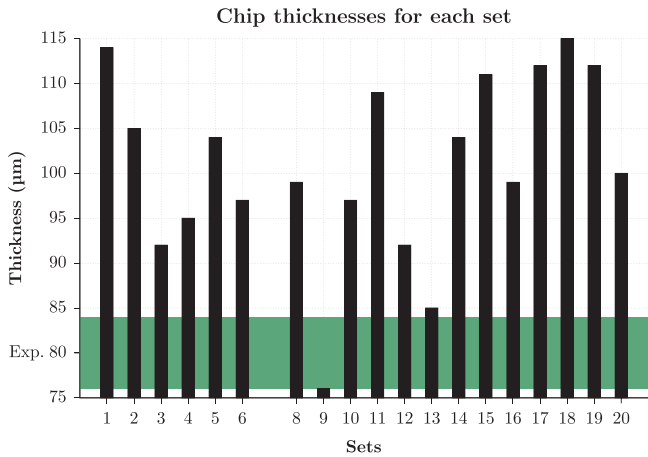Fig. 25. Temperature contours (in K) of the numerical chips of sets 1, 9 and 20 for $h = 60\,\mu m$ after 600 µs of cutting.

Fig. 26. Numerical and experimental chip thicknesses for $h = 60\,\mu m$ after 600 µs of cutting (the experimental reference is shown with its standard deviation interval).

Table 6
RMS cutting forces and chip thickness summary for $h = 40\,\mu m$, Δ_x: difference with the experimental values.

Case	CF (N/mm)	Δ_{CF} (%)	FF (N/mm)	Δ_{FF} (%)	h' (µm)	$\Delta_{h'}$ (%)
Exp.	86 ± 2	–	40 ± 1	–	59 ± 5	–
Set 9	77	11	48	−20	52 ± 1	12
Set 15	116	−35	43	−7	73 ± 1	−24
Set 16	84	2	36	9	67 ± 1	−14

Table 7
RMS cutting forces and chip thickness summary for $h = 100\,\mu m$, Δ_x: difference with the experimental values.

Case	CF (N/mm)	Δ_{CF} (%)	FF (N/mm)	Δ_{FF} (%)	h' (µm)	$\Delta_{h'}$ (%)
Exp.	174 ± 2	–	50 ± 1	–	135 ± 6	–
Set 9	155	11	47	5	124 ± 2	8
Set 15	244	−40	32	36	≈184	≈ − 36
Set 16	171	2	31	38	165 ± 1	−22

as the decrease of the maximal temperature in the secondary shear zone with the cutting force RMS value. The temperature in the secondary shear zone of chips 5, 6, 12 and 13 (Fig. 24) are low, and particularly for chip 6, which is due to its low cutting force RMS value.

The characteristics of chip 20 (Fig. 25) are medium, as well as its forces and flow stress. Chip 1 (Fig. 25) is very thick and its feed force is consequently very low (similarly to its low flow stress level). The temperatures in the secondary shear zone are low as well, in direct link with its cutting force and flow stress. The thickness of chip 9 (Fig. 25) is the smallest, while its RMS feed force is the largest. This confirms what has been observed with the other sets. The temperatures in the secondary shear zone are rather low like its cutting force and flow stress levels. The n value of chip 9 is the lowest which leads to a flow stress nearly independent of the strain when it is above 0.5. This flow stress shape produces a thin chip. Most of the other chips with a thickness in the lower range do not have a large n value. On the contrary, the thick chips such as 7, 17, 18 or 19 have a large n value. There is therefore a direct link between the n value and the chip thickness.

The comparison with the experimental value (Fig. 26) shows that all the numerical chips, except chip 9, have a thickness larger than the reference. Only chips 9 and 13 are close to the experimental reference.

the secondary shear zone carry on their decrease with the cutting force. The secondary shear zone is still however the area where the temperature is the highest.

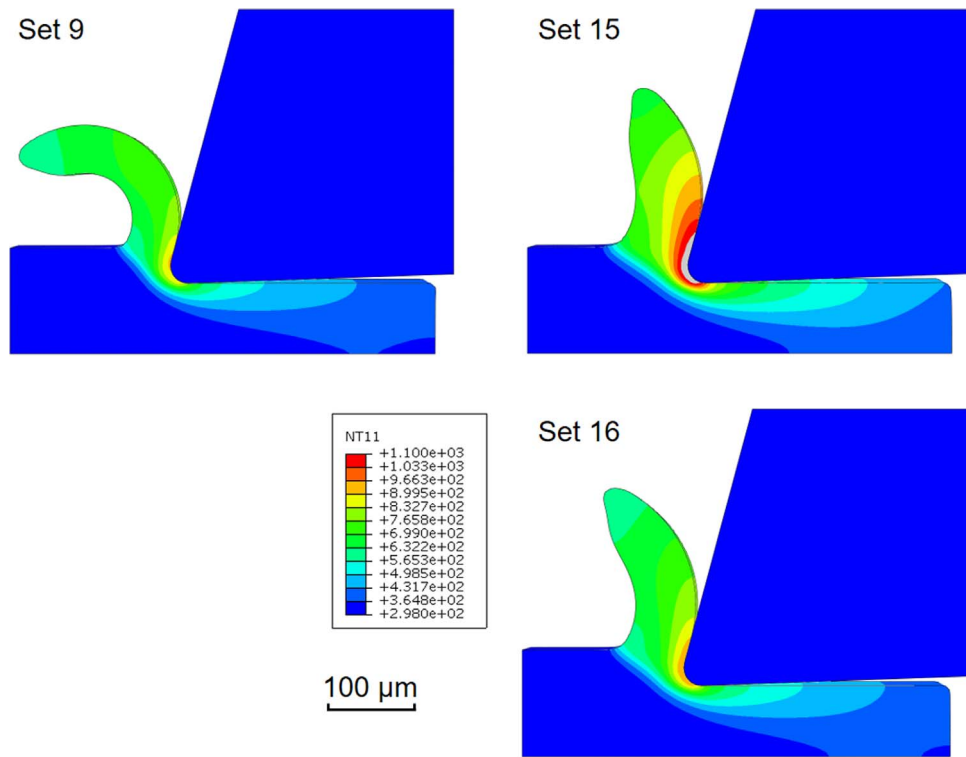The inverse link between the chip thickness and the feed force RMS value is again clearly observed for chips 11, 14 and 16 (Fig. 23), as well

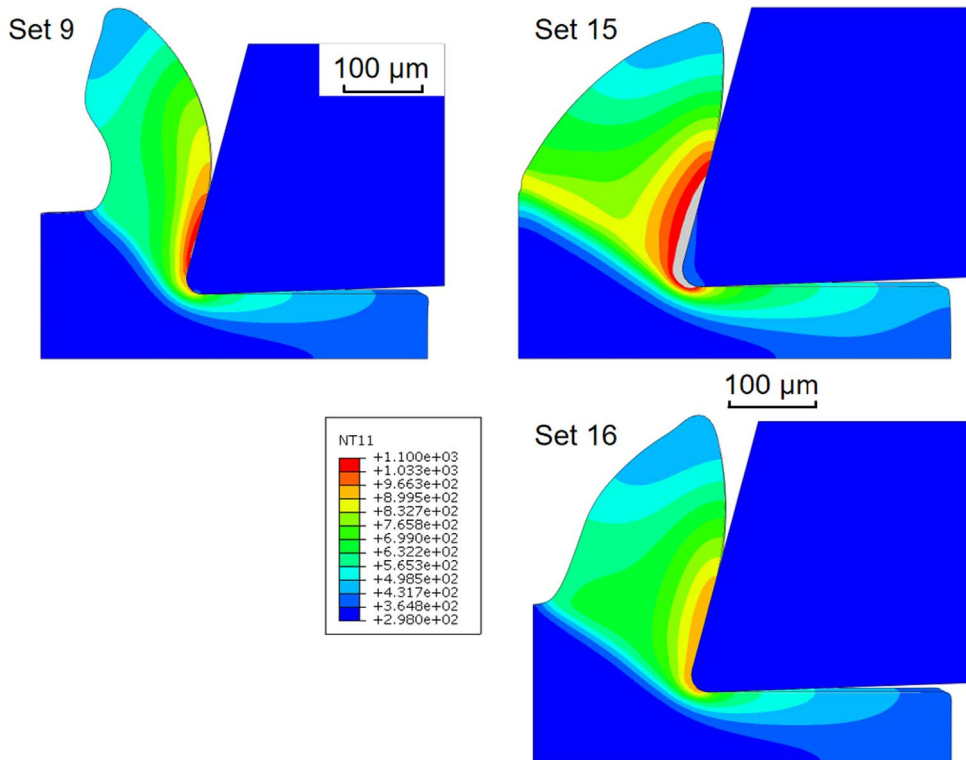Fig. 27. Temperature contours (in K) of the numerical chips of sets 1, 9 and 20 for $h = 40$ μm after 600 μs of cutting.

Fig. 28. Temperature contours (in K) of the numerical chips of sets 1, 9 and 20 for $h = 100$ μm after 600 μs of cutting.

6.3. Conclusions

To conclude the comparison between the twenty Johnson-Cook sets of parameters and the experimental reference, it can be said that there is not a unique set that allows to correctly predict the cutting force, the feed force and the chip thickness. This was already mentionned in the literature review [16,17]. The cutting force is the most used output of a numerical model because it is industrially important and it turned out to be the best modelled. The experimental cutting force value is close to the average value of all the sets. The feed force and the chip thickness are on the contrary less well modelled. The feed force is nearly always underestimated, while the chip thickness is overestimated. The set of Johnson-Cook parameters to recommend in order to obtain good finite element results is set 16. Its cutting force RMS value is as accurately

estimated as set 14 but set 16 models better the feed force and the chip thickness. The feed force and chip thickness were however not particularly well modelled by set 16 but their values are in the middle of the ranges.

7. Other uncut chip thicknesses

Two other cutting conditions are now considered to check if the trends previously highlighted are still valid. The cutting conditions are an uncut chip thickness of 40 μm and 100 μm with all the other parameters unchanged, in order to adopt the same conditions as in the experiments. Three different sets of Johnson-Cook parameters are used. The first one is set 16 because it turned out to be the recommended set at $h = 60$ μm. It provided the best estimation of the cutting force and the feed force and chip thickness values were in the middle of the numerical ranges of values. The two other sets give more extreme outputs values. They were chosen on purpose to highlight the influence of the parameters on the numerical results. The second set is 9 because it formed the thinnest chip and resulted in the highest feed force. Set 15 is the third one. After sets 7 and 18, which have a distinctive flow stress, set 15 provided the highest cutting force value and one of the thickest chips.

The results for the cutting force show the same trend at $h = 40$ μm (Table 6) and $h = 100$ μm (Table 7) than at $h = 60$ μm (Table 5). Set 16 provides a value equal to the experimental reference (including the experimental standard deviation). Set 9 slightly underestimates the cutting force, while set 15 considerably overestimates it. For the feed force, the observations are different for $h = 40$ μm and $h = 100$ μm. When $h = 100$ μm, set 9 provides the best feed force value, followed by set 15 and then set 16 as at $h = 60$ μm. For $h = 40$ μm, set 9 largely overestimates the feed force as when $h = 60$ μm. Set 15 overestimates it as well but its value is close to the reference one. Set 16 underestimates the feed force but the difference with the reference is smaller than at the other uncut chip thicknesses. This ends in a feed force value roughly estimated by set 9 although it provided the best values at $h = 40$ μm and $h = 60$ μm. The trend on the values is however maintained as the highest feed force is from set 9 and the lowest from set 16.

The chips morphologies are shown in Figs. 27 and 28. The trend is the same for both uncut chip thicknesses at 60 μm. The chip of set 9 is the thinnest (Tables 6 and). Both sets 15 and 16 provide a thicker chip (Tables 6, 7) and chip 16 is closer to the reference than chip 15. At $h = 40$ μm, the chips thicknesses of set 9 and set 16 are both quite close to the reference. At $h = 100$ μm, the differences for the three chips are close to what was observed at $h = 60$ μm. It must be noted in Table 7 that the chip thickness value should only be considered as an estimation for set 15: its chip has not reached the steady-state yet (Fig. 28). This is however enough to extract trends. Surprisingly, the feed forces values are not the highest for the largest uncut chip thickness, which is not realistic. When looking close to the feed forces and the chips morphologies, it turns out that this is due to the shape of the chips, as a thicker chip will lead to a lower RMS feed force value. The more the chip thickness is overestimated, the more the feed force is underestimated, ending in feed forces values that can be smaller for a larger uncut chip thickness. The highest temperature is still in the secondary shear zone. The trends observed at $h = 60$ μm are therefore maintained when $h = 40$ μm and 100 μm.

In conclusion of this analysis for the three selected sets of Johnson-Cook parameters, the trends are the same at the three uncut chip thicknesses and the cutting force is the best estimated output.

8. Conclusions

The influence of the choice of a set of parameters for the Johnson-Cook constitutive model on the results of an orthogonal cutting model has been studied extensively with twenty different sets of parameters for Ti6Al4V. It results of this study that:

- Significant differences in the values of the parameters of the sets of the Johnson-Cook constitutive model for Ti6Al4V are observed in the sets available in the literature. This ends in very different stresses values although the same material is considered.
- The information provided in the literature when the Johnson-Cook parameters are identified are often not complete. This concerns the experimental conditions of the tests, as well as the thermal treatments history of the alloy.
- The cutting force is the best modelled output. The feed force is usually underestimated and the chip thickness is overestimated.
- A direct link can be made between the level of the flow stress, the RMS value of the cutting force and the temperature in the secondary shear zone, as well as between the value of n and the chip thickness. The chip thickness and the RMS value of the feed force are inversely linked.
- The highlighted trends have been confirmed for two other uncut chip thicknesses with a selection of three sets of Johnson-Cook parameters.
- The set of Johnson-Cook parameters from Seo et al. [33] gives accurate results for the cutting force and estimates averagely the feed force and the chip thickness. This set is therefore recommended for finite element modelling of Ti6Al4V orthogonal cutting.

References

[1] Ducobu F, Rivière-Lorphèvre E, Filippi E. Application of the Coupled Eulerian-Lagrangian (CEL) method to the modeling of orthogonal cutting. Eur J Mech - A/ Solids 2016;59:58–66.

[2] Jeunechamp P-P. Simulation numérique, à l'aide d'algorithmes thermomécaniques implicites, de matériaux endommageables pouvant subir de grandes déformations. Application aux structures aéronautiques soumises à impact, [Ph.D. thesis], Université de Liège, 2008.

[3] Hor A. Simulation physique des conditions thermomécaniques de forgeage et d'usinage - Caractérisation et modélisation de la rhéologie et de l'endommagement. [Ph.D. thesis], Arts et Métiers ParisTech - Centre d'Angers, 2011.

[4] Pantalé O. Plateforme de prototypage virtuel pour la simulation numérique en Grandes Transformations Thermomécaniques Rapides. Technical Report, Institut National Polytechnique de Toulouse, 2005.

[5] Poulachon G, Moisan A, Jawahir I. Comportement, propriétés et usinabilité des aciers durcis - Tournage dur de l'acier è roulement 100Cr6. Matériaux 2002;2002.

[6] Johnson G, Cook W. A constitutive model and data for metals subjected to large strains, high strain rates and high temperatures. In: Proceedings of the seventh international symposium on ballistics, The Hague, The Netherlands 1983 541–547.

[7] Ducobu F, Arrazola P-J, Rivière-Lorphèvre E, Filippi E. Comparison of several behaviour laws intended to produce a realistic Ti6Al4V chip by finite elements modelling. Key Eng 2015;651–653:1197–203.

[8] Chen G, Ren C, Yang X, Jin X, Guo T. Finite element simulation of high-speed machining of titanium alloy (ti-6al-4v) based on ductile failure model. Int J Adv Manuf Technol 2011;56:1027–38.

[9] Zhang Y, Mabrouki T, Nelias D, Gong YD. Chip formation in orthogonal cutting considering interface limiting shear stress and damage evolution based on fracture energy approach. Finite Elem Anal Des 2011;47:850–63.

[10] Miguèlez M, Soldani X, Molinari A. Analysis of adiabatic shear banding in orthogonal cutting of Ti alloy. Int J Mech Sci 2013;75:212–22.

[11] Kolsky H. An Investigation of the Mechanical Properties of Materials at very High Rates of Loading. In: Proceedings of the physical society B 62; 1949 676–700.

[12] Calamaz M, Coupard D, Girot F. A new material model for 2D numerical simulation of serrated chip formation when machining titanium alloy Ti-6Al-4V. Int J Mach Tools Manuf 2008;48:275–88.

[13] Sima M, Özel T. Modified material constitutive models for serrated chip formation simulations and experimental validation in machining of titanium alloy Ti-6Al-4V. Int J Mach Tools Manuf 2010;50:943–60.

[14] Arrazola P, Özel T. Investigations on the effects of friction modeling in finite element simulation of machining. Int J Mech Sci 2010;52:31–42.

[15] Özel T. The influence of friction models on finite element simulations of machining.

Int J Mach Tools Manuf 2006;46:518–30.

[16] Filice L, Micari F, Rizzuti S, Umbrello D. Dependence of machining simulation effectiveness on material and friction modelling. Mach Sci Technol: Int J 2008;12:370–89.

[17] Umbrello D, M'Saoubi R, Outeiro J. The influence of Johnson-Cook material constants on finite element simulation of machining of AISI 316L steel. Int J Mach Tools Manuf 2007;47:462–70.

[18] Umbrello D. Finite element simulation of conventional and high speed machining of Ti6Al4V alloy. J Mater Process Technol 2008;196:79–87.

[19] Tounsi N, Vincenti J, Otho A, Elbestawi M. From the basic mechanics of orthogonal metal cutting toward the identification of the constitutive equation. Int J Mach Tools Manuf 2002;42:1373–83.

[20] Khan A, Suh Y, Kazmi R. Quasi-static and dynamic loading responses and constitutive modeling of titanium alloys. Int J Plast 2004;20:2233–48.

[21] Klopp R, Clifton R, Shawki T. Pressure-shear impact and the dynamic viscoplastic response of metals. Mech Mater 1985;4:375–85.

[22] Lee W, Lin C. Plastic deformation and fracture behaviour of Ti-6-4V alloy loaded with high strain rate under various temperatures. Mater Sci Eng A 1998;241:48–59.

[23] Lee W, Lin C. High-temperature deformation behaviour of Ti6Al4V alloy evaluated by high strain-rate compression tests. J Mater Process Technol 1998;75:127–36.

[24] Özel T, Zeren E. Identification of constitutive material models parameters for high-strain rate metal cutting conditions using evolutionary computational algorithms. Mater Manuf Process 2007;22:659–67.

[25] Özel T, Zeren E. Determination of work material flow stress and friction for FEA of machining using orthogonal cutting tests. J Mater Process Technol 2004;153–154:1019–25.

[26] Johnson G. Strength and Fracture Characteristics of a Titanium Alloy (.06Al,.04 V) Subjected to Various Strains, Strain Rates, Temperatures and Pressures. Technical Report, NSWC TR 86-144, Dahlgren, VA; 1985.

[27] Dumitrescu M, Elbestawi M, El-Wardany T. Mist coolant applications in high speed machining of advanced materials metal cutting and high speed machining. Kluwer Academic: Plenum Publishers; 2002. p. 329–39.

[28] Bois D, Grave A. Simulation numérique d'essais d'impact et comparaison de lois de comportment. J De Phys 1985;46:101–8.

[29] Meyer HW, Kleponis DS. Modeling the high strain rate behavior of titanium undergoing ballistic impact and penetration. Int J Impact Eng 2001;26:509–21.

[30] Li L, He N. A FEA study on mechanisms of saw-tooth chip deformation in high speed cutting of Ti-6-Al-4V alloy. In: Proceedings of the fifth international conference on high speed machining (HSM); 2006, 759–767.

[31] Bouchnak TB. Etude du comportement en sollicitations extrêmes et de l'usinabilité d'un nouvel alliage de titane aéronautique: le Ti555-3. [Ph.D. thesis], Arts et Mtiers ParisTech - Centre de Angers; 2010.

[32] Macdougall D, Harding J. A constitutive relation and failure criterion for Ti5Al3V alloy at impact rates of strain. J Mech Phys Solids 1999;47:1157–85.

[33] Seo S, Min O, Yang H. Constitutive equation for Ti-6Al-4V at high temperatures measured using the SHPB technique. Int J Impact Eng 2005;31:735–54.

[34] Kay G. Failure modeling of titanium Ti6Al4V and aluminium 2024-T3 with the Johnson-Cook material model. Technical Report, U.S. Department of Energy, Lawrence Livermore National Laboratory; 2002.

[35] Nemat-Nasser S, Guo W, Nesterenko V, Indrakanti S, Gu Y. Dynamic response of conventional and hot isostatically pressed Ti-6Al-4V alloys: experiments and modeling. Mech Mater 2001;33:425–39.

[36] Ducobu F, Rivière-Lorphèvre E, Filippi E. Experimental contribution to the study of the Ti6Al4V chip formation in orthogonal cutting on a milling machine. Int J Mater Form 2015;8:455–68.

[37] H.K.S., Abaqus Analysis User's Manual. Version 6.14, Dassault Systèmes; 2014.

[38] Rech J, Arrazola P, Claudin C, Courbon C, Pusavec F, Kopac J. Characterisation of friction and heat partition coefficients at the tool-work material interface in cutting. CIRP Ann - Manuf Technol 2013;62:79–82.

[39] Özel T, Zeren E. Numerical modelling of meso-scale finish machining with finite edge radius tools. Int J Mach Mach Mater 2007;2:451–768.

[40] Sun J, Guo YB. Material flow stress and failure in multiscale machining titanium alloy Ti-6Al-4V. Int J Adv Manuf Technol 2009;41:651–9.

[41] Lampman S. Wrought titanium and titanium alloys, properties and selection: Nonferrous alloys and special-purpose materials. ASM Handbook, ASM International 2; 1990, 592–633.

[42] Nasr M, Ng E-G, Elbestawi M. Effects of workpiece thermal properties on machining-induced residual stresses - thermal softening and conductivity. in: Proceedings of the institution of mechanical engineers, part b: journal of engineering manufacture 221; 2007, pp. 1387–1400.